

1 Ultra-oxidized rocks in subduction mélanges? Decoupling
2 between oxygen fugacity and oxygen availability in a Mn-rich
3 metasomatic environment

4 **Simone Tumiatia*, Gaston Godardb, Silvana Martinc, Nadia Malaspina^d and Stefano Poli^a**

5 *^a Dipartimento di Scienze della Terra “Ardito Desio”, Università degli Studi di Milano, via
6 Mangiagalli 34, I-20133 Milano, Italy; simone.tumiati@unimi.it*

7 *^b Institut de Physique du Globe de Paris, Sorbonne Paris Cité, Université Paris Diderot, UMR 7154
8 CNRS, 1 rue Jussieu, F-75252 Paris, France*

9 *^c Dipartimento di Geoscienze, Università degli Studi di Padova, via Giotto 1, 35137 Padova, Italy*

10 *^d Dipartimento di Scienze dell’Ambiente e del Territorio e di Scienze della Terra, Università degli
11 Studi di Milano Bicocca, piazza della Scienza 4, 20126 Milano, Italy*

12

13 **ABSTRACT**

14 The manganese ore of Praborna (Italian Western Alps) is embedded within a metasedimentary
15 sequence belonging to a subduction mélange equilibrated at high-pressure (HP) conditions (ca. 2
16 GPa) during the Alpine orogenesis. The pervasive veining of the ore and the growth of “pegmatoid”
17 HP minerals suggest that these Mn-rich rocks strongly interacted with slab-derived fluids during HP
18 metamorphism. These rocks are in textural and chemical equilibrium with the veins and in contact
19 with sulphide- and magnetite-bearing metabasites at the bottom of the sequence. They contain
20 braunite ($\text{Mn}^{2+}\text{Mn}^{3+}_6\text{SiO}_{12}$), quartz, pyroxmangite ($\text{Mn}^{2+}\text{SiO}_3$), and minor hematite, omphacite,
21 piemontite and spessartine-rich garnet. Sulphides are absent in the Mn-rich rocks, whereas
22 sulphates (barite, celestine) occur together with As- and Sb-oxides and silicates. This rock
23 association provides an excellent natural laboratory to constrain the redox conditions in subducting
24 oceanic slab mélanges at HP and fluid-present conditions. Similarly to Fe-bearing minerals, Mn

25 oxides and silicates can be regarded as natural redox-sensors. A thermodynamic dataset for these
26 Mn-bearing minerals is built, using literature data as well as new thermal expansion parameters for
27 braunite and pyrolusite, derived from experiments. Based on this dataset and the observed
28 assemblages at Praborna, thermodynamic calculations show that these mélangé rocks are
29 characterized by ultra-oxidized conditions (ΔFMQ up to +12.7) if the chemical potential of oxygen
30 (or the oxygen fugacity $f\text{O}_2$) is accounted for. On the other hand, if the molar quantity of oxygen is
31 used as the independent state variable to quantify the bulk oxidation state, the ore appears only
32 moderately oxidized and comparable to typical subduction-slab mafic eclogites. Such an apparent
33 contradiction may happen in rock systems whenever oxygen is improperly considered as a perfectly
34 mobile component. In the Earth's mantle, redox reactions take place mainly between solid oxides
35 and silicates, because O_2 is a negligible species in the fluid phase. Therefore, the description of the
36 redox conditions of most petrological systems requires the introduction of an extensive variable,
37 namely the oxygen molar quantity ($n\text{O}_2$). As a consequence, the oxygen chemical potential, and
38 thus $f\text{O}_2$, becomes a dependent state variable, not univocally indicative of the redox conditions of
39 the entire rock column of a subduction zone, from the dehydrating oceanic crust to the overlying
40 mantle wedge. On a more general basis, the comparison of $f\text{O}_2$ retrieved from different bulk
41 compositions and different phase assemblages is sometimes challenging and should be undertaken
42 with care. From the study of mélangé rocks at Praborna, the distribution of oxygen at subduction
43 zones could be modelled as an oxidation gradient, grading from a maximum in the subducted
44 altered oceanic crust to a minimum in the overlying peridotites of the mantle hanging-wall.

45

46 **Keywords:** manganese, oxidation, oxygen fugacity, subduction, mantle wedge, slab, eclogite

47

48 **Highlights:**

- 49 • The manganese-rich rocks of Praborna are high-pressure metacherts belonging to a slab
50 mélangé.

- 51 • Rocks are veined pervasively suggesting a strong interaction at HP with slab-derived fluids.
- 52 • Mn-rich mineral associations suggest ultra-high fO_2 conditions up to $\Delta FMQ +12.7$.
- 53 • In terms of quantity of O_2 , the same rocks display a moderate oxidation state.
- 54 • The decoupling between intensity and extensity of O_2 in metasomatic rocks is highlighted.

55

56 **1. Introduction**

57 The reduction-oxidation (redox) conditions of rocks are known to affect phase relationships,
58 speciation of volatile elements, trace element partitioning, diffusivity, electrical conductivity and
59 mechanical properties (Arculus, 1985). Redox conditions are traditionally described using the
60 intensive variable oxygen fugacity (fO_2). Variability in fO_2 at subduction zones has been debated
61 since a long time (Gill, 1981; Wood et al., 1990; Foley et al., 2011). Compared to the
62 asthenospheric and lithospheric mantles, relatively high fO_2 has been proposed for subducted slab
63 materials, sub-arc mantle and arc magmas (Hirschmann, 2009; Kelley and Kottrell, 2009;
64 Malaspina et al., 2009, 2010; Groppo and Castelli, 2010; Evans, 2012). However, trace-element and
65 isotope systematics, aimed to constrain the variation of fO_2 in the mantle (Canil, 2002; Lee et al.,
66 2005, 2010), challenge such conclusion, emphasizing a discrepancy between the fO_2 calculated by
67 oxygen thermobarometry and that inferred from V/Sc data on arc lavas.

68 The redox conditions of rocks could be also expressed in terms of ratios of cations occurring in
69 different oxidation states, such as Fe^{2+} and Fe^{3+} . However, paucity of thermodynamic data on Fe^{3+}
70 end-members of minerals and analytical difficulties in retrieving Fe^{3+}/Fe^{2+} in fine-grained,
71 texturally complex volatile-rich rocks have hindered so far the quantitative assessment of redox
72 conditions in the slab-mantle mixing zone in terms of Fe^{3+}/Fe^{2+} ratio (Bebout, 2007). On the other
73 hand, Mn-rich nodules and crusts, though volumetrically very limited, are nearly ubiquitous on the
74 seafloor (Manheim, 1978) and contain highly oxidized Mn^{4+} -bearing phases, such as amorphous
75 MnO_2 , pyrolusite, birnessite, and todorokite (e.g., Ostwald and Frazer, 1973). Upon metamorphism,
76 a variety of Mn^{3+} and Mn^{2+} oxides and silicates may form in subduction mélanges, depending on P -

77 T - X conditions (e.g., Dasgupta, 1997; Tumiati et al., 2010). The variable oxidation states of
78 manganese make Mn minerals extremely useful sensors to constrain redox conditions of rocks.
79 The present study takes advantage of the manganese ore of Praborna, cropping out in the Italian
80 western Alps, and consisting of Mn-rich metasediments embedded within meta-ophiolites (Tumiati
81 et al., 2010). This ore displays a complex variety of Mn- and Fe-rich mineral assemblages, formed
82 at eclogite-facies conditions in a subduction mélange. Swarms of stockwork high-pressure (HP)
83 veins are cutting the Mn-rich rocks, suggesting an interaction with slab-derived fluids at very high
84 fluid-rock ratio, as expected for such very thin, veined, metasedimentary sequences (Bebout et al.,
85 2013). Praborna represents an excellent natural laboratory for the study of the behaviour of the
86 component oxygen in terms of mobility in oceanic slab mélanges subducted at HP conditions and
87 flushed by fluids. This particular case should be considered as paradigmatic, because it draws the
88 attention to the choice of the independent parameter capable of describing the redox conditions of
89 rocks in a metasomatic environment.

90

91 **2. Concepts and definitions**

92 Oxidation and reduction are defined in general chemistry as loss and gain of electrons, respectively.
93 Since oxygen is the most common electron acceptor in natural systems, because of its high
94 electronegativity, oxidation and reduction generally mean gain and loss of oxygen, by exchange
95 with the external medium. Thus, the redox condition of rocks is described by considering a variable
96 that can potentially rule this exchange. Exception done for a few works (e.g., Chinner, 1960; Evans,
97 2006), the variable traditionally considered in Earth sciences is the oxygen fugacity (fO_2). However,
98 O_2 is not expected to be a major gaseous/fluid species in the Earth's interior, and the chemical
99 potential of oxygen (either μO or μO_2) could appear more appropriate. In this study, we use both
100 variables fO_2 and μO_2 considered as equivalent.

101 The fugacity of a gaseous species is the theoretical partial pressure that this gas would have if it
102 would obey the ideal-gas law ($P \times V = n \times R \times T$). This means that fugacity is equal to partial

103 pressure only in ideal gases (i.e., for $P \rightarrow 0$ bar). At higher pressures, gases strongly diverge from
104 the ideal gas law, and a fugacity coefficient ($\phi = f/P$) is introduced accounting for the non-ideal
105 behaviour. The fugacity of a gas is in turn a function of the chemical potential of the relative
106 component. For the component O_2 , this relationship is expressed by the following equation:

$$107 \quad \mu_{O_2} = G_{f,T,O_2}^0 + R \times T \times \ln f_{O_2}/f^0_{O_2}$$

108 where

- 109 • μ_{O_2} ($J \cdot mol^{-1}$) is the chemical potential of the component O_2 at P and T of interest;
- 110 • G_{f,T,O_2}^0 ($J \cdot mol^{-1}$) is the molar Gibbs energy of formation of pure oxygen (O_2) at $P^0 = 1$ bar
111 and T ;
- 112 • R ($J \cdot K^{-1} \cdot mol^{-1}$) is the gas constant;
- 113 • f_{O_2} (bar) is the fugacity of pure oxygen at P and T of interest;
- 114 • $f^0_{O_2}$ is the fugacity of pure oxygen at the standard-state pressure P^0 ($f^0_{O_2} = 1$ bar at all T).

115 As for any other component of a petrological system, μ_{O_2} , and thus f_{O_2} , is ideally homogenous in
116 all phases at equilibrium and independent of the phase abundance; in other terms, it is an intensive
117 variable. The O_2 molar quantity (n_{O_2}) is the conjugate extensive variable of μ_{O_2} , since the product
118 ($\mu_{O_2} \times n_{O_2}$) has the dimension of an energy ($J \cdot mol^{-1} \times mol = J$), similarly to other couples of
119 intensive and extensive variables like ($P \times V$) and ($T \times -S$).

120 While considering an oxidised system, the set of basis vectors that generate the compositional
121 vector space (i.e. the set of independent components) could be either $\{Si, Fe, Mn, \dots, O\}$ or $\{SiO_2,$
122 $FeO, MnO, \dots, O_2\}$. We have chosen here the latter set of independent components, so that μ_{O_2} and
123 n_{O_2} have to be considered instead of μ_O and n_O . In that case, n_{O_2} represents the coordinate for the
124 basis vector O_2 ; it equals zero when all Fe and Mn occur in their divalent oxidation state, i.e. as FeO
125 and MnO (see Fig. 7).

126 The choice to describe a redox system in terms of intensive variables (f_{O_2} or μ_{O_2}) is entirely valid
127 only if O_2 can be considered a “perfectly mobile” component. As already explained by Korzhinskii
128 (1959, p. 16), the behaviour of a chemical component in a rock system could be “inert” or

129 “perfectly mobile”, depending on its mobility between the system and an external medium. As an
130 example, during a fluid-rock interaction, where the system is the rock and the external medium is a
131 fluid phase flushing the rock, those rock components that are not readily transported by the fluid are
132 considered inert or “immobile”, whereas components that can dissolve into the fluid can be
133 considered “mobile” and rapidly react with the surrounding rock. On this principle, the quantity of
134 inert components has a fundamental role to attain the equilibrium, while it can be neglected for
135 mobile components. Therefore, from a thermodynamic point of view, during the equilibration
136 between a rock and a fluid phase, the molar quantity of material should be considered as an
137 independent state variable for inert components, whereas chemical potential must be used as an
138 independent state variable for perfectly mobile components (Korzhinskii, 1959).

139 A complication arises when we consider the component O_2 in the Earth’s interior, because redox
140 reactions take place mainly between solid oxides and silicates, where oxygen is bonded to relatively
141 inert components such as FeO (forming, for example, Fe_2O_3) and MnO (forming, for example,
142 Mn_2O_3), while it occurs in very limited amounts in fluids. Therefore, O_2 cannot be considered
143 unequivocally a perfectly mobile component. It could well be that, in many cases, O_2 is better
144 regarded as an inert component, so that n_{O_2} , rather than μ_{O_2} , becomes an independent
145 thermodynamic state variable imposed upon the system.

146 Considering the variable n_{O_2} instead of μ_{O_2} modifies the inspection of phase relationships (e.g.,
147 Hillert, 1985). In particular, when a molar quantity is introduced as an axis instead of its conjugate
148 chemical potential, two one-phase fields will separate from each other, thus leaving room for the
149 two-phase field, and their distance will be equal to the difference in the molar quantity between the
150 two phases (Fig. 1). In addition, when molar quantities other than n_{O_2} are not constant, μ_{O_2} (and
151 f_{O_2}) is not a simple, monotonically increasing function of the quantity of oxygen. Therefore, the
152 reconstruction of the extensive property (n_{O_2}) from the intensive variable (f_{O_2} or μ_{O_2}) can be a
153 very inaccurate procedure in natural, multi-component systems (see Malaspina et al., 2009, 2012).

154

155 **3. The Praborna manganese ore**

156 Slices of Mn-rich metasediments are commonly hosted in meta-ophiolites of the Western Alps.
157 Praborna (Saint-Marcel valley, Italy; Fig. 2) is the largest Mn deposit in the Zermatt-Saas unit,
158 which is interpreted as part of the Jurassic oceanic lithosphere of the Tethys, subducted during the
159 Alpine orogeny (e.g., Dal Piaz, 2001). In the Zermatt-Saas unit, Mn-rich rocks from Lago di
160 Cignana (Valtournanche) preserve coesite (Reinecke, 1998) and microdiamonds (Frezzotti et al.,
161 2011), suggesting that the oceanic sediments underwent ultrahigh-*P* (UHP) metamorphism. HP
162 metamorphic peak conditions of 2.1 GPa and 550 °C were recorded also in the meta-ophiolite of the
163 Saint-Marcel valley (Martin et al., 2008), which are the country rocks of the Praborna deposit.
164 The disused mine of Praborna, known since 1415 CE (Castello, 1982), is world-famous for its
165 peculiar rocks and minerals. In particular, it is the type locality of five mineralogical species,
166 namely piemontite, braunite, romeite, strontiomelane, and manganiandrosite-(Ce) (Ciriotti et al.,
167 2009 and references therein). The Praborna deposit displays a continuous change in mineralogy
168 from the basal contact with metabasites (now glaucophanites) towards the upper contact with Mn-
169 poor metasediments (Figs. 2, 3), and consists of boudinaged Mn-rich metasediments cropping out in
170 a “mélange” composed of serpentinite, ophicarbonates breccias, metagabbro and metabasalt with N-
171 MORB affinity (Fig. 2; Martin and Kienast, 1987; Martin et al., 2008; Tumiati et al., 2010).
172 Swarms of stockwork HP veins cut the Mn-rich rocks especially near the basal contact (Fig. 3),
173 suggesting an interaction with slab-derived fluids. On the basis of the mineralogical composition,
174 several “levels” have been recognized (Martin and Kienast, 1987; Tumiati et al., 2010). Basal levels
175 and veins contain braunite (the ore mineral), piemontite and jadeite-rich Mn-bearing omphacite,
176 whereas upper levels are characterised by the abundance of garnet ± pyroxmangite ± jadeite-poor
177 clinopyroxene. Quartz is generally abundant in all the levels. In Table 1, we report representative
178 mineral compositions of the basal and upper levels, the HP veins and the SiO₂-undersaturated
179 assemblages found at Praborna. Other details concerning mineralogy and petrography of the ore are
180 provided in Section 5, as Supplementary Material (SM), and in Tumiati et al. (2010).

181

182 **4. Materials and methods**

183 Several thin sections of the basal and upper levels (Table SM-1 in the Supplementary Material)
184 have been analysed at the petrographic and scanning electron microscopes. Chemical analyses
185 reported in Table 1 were performed using the Cameca SX100 (Paris) and JEOL 8200 (Milano)
186 wavelength-dispersive electron microprobes (EMP), at 15-kV accelerating potential, 15-nA sample
187 current and 1- μ m beam diameter. Standards used were albite (Na), diopside (Ca, Mg and Si), Fe₂O₃
188 (Fe), orthoclase (Al and K), MnTiO₃ (Mn and Ti), Cr₂O₃ (Cr) and barite (Ba). A counting time of
189 30 s was applied for all elements.

190 The Fe³⁺/Fe_{TOT} and Mn³⁺/Mn_{TOT} ratios in minerals have been calculated by stoichiometry. Because
191 of the relative electronegativity of Fe and Mn, the pair Fe³⁺-Mn²⁺ is more stable than the pair Fe²⁺-
192 Mn³⁺, which has never been reported in minerals (Sherman, 1990). In fact, values of standard redox
193 potential (or electromotive force) are 0.77 V for the pair Fe³⁺-Fe²⁺ and 1.51 V for Mn³⁺-Mn²⁺.
194 Therefore, the charges were calculated iteratively, by adjusting first Fe³⁺/Fe_{TOT}, and then, if
195 necessary, Mn³⁺/Mn_{TOT}. In any case, this study is mainly focused on simple manganese oxides and
196 silicates characterized by fixed Mn³⁺/Mn_{TOT}, so that uncertainties related to this procedure do not
197 affect the conclusions provided here.

198 For more complex phases, crystal chemistry has been evaluated mostly using the principal
199 component analysis (PCA). In particular, this method was used to unravel substitution vectors in
200 solid solutions. PCA is a statistical procedure that transforms a number of possibly correlated
201 variables into the same number of uncorrelated variables given by the eigenvectors of the
202 covariance matrix, and called principal components. The first principal component (F1) account for
203 as much of the variability in the data as possible, and thus corresponds to the highest eigenvalue of
204 the covariance matrix; each of the succeeding components (F2, F3...) accounts for as much of the
205 remaining variability as possible. For other details and examples of PCA applied to EMP data, refer
206 to Tumiati et al. (2005 A, 2005 B, 2008, 2013).

207 Raman spectroscopy of selected samples has been carried out using a green (514 nm) laser
208 radiation, at the *Muséum National d'Histoire Naturelle* of Paris. In particular, Raman spectroscopy
209 was required for the identification of the HP MnSiO₃ polymorph pyroxmangite.

210

211 **5. Mineralogy and petrography of the Praborna ore**

212 *5.1 Basal levels*

213 The basal levels (Fig. 3; Table 1) are in contact with glaucophanite made up of glaucophane +
214 garnet + chloritoid + chlorite + paragonite and showing pseudomorphs after lawsonite (Martin et
215 al., 2008). These basal levels mainly contain braunite (Mn²⁺Mn³⁺₆SiO₁₂) and piemontite (Fig. 3),
216 minor quartz, omphacite, garnet, phengite and pyroxmangite, the HP polymorph of Mn²⁺SiO₃ (Fig.
217 4A; see Raman spectrum of sample SM93 in Fig. 5). Hematite is the stable iron oxide (Fig. 4a),
218 while magnetite was never observed. Rutile and As-bearing apatite (Fig. 6a) are common
219 accessories. Sulphides were not observed, although they are reported in the host metabasites of the
220 Saint-Marcel valley, where Fe–Cu ores have been exploited in the past centuries (mines of Servette
221 and Chuc; e.g. Martin et al., 2008; Tumiati et al., 2008).

222 Omphacite in these levels is dark purple and known as a semiprecious stone called *violan* (Bondi et
223 al., 1978). It is a solid solution of jadeite (up to Jd₆₄), diopside and aegirine, with minor contents in
224 johansennite (CaMn²⁺Si₂O₆) and namansilite (NaMn³⁺Si₂O₆), often showing a complex zoning.
225 PCA indicates that the main substitution vector in omphacite, represented by the first principal
226 component F1 (79.55 % of the total eigenvalues), concerns augite (elements Ca, Mg, Fe²⁺, Mn²⁺)
227 vs. jadeite + aegirine + namansilite (elements Na, Al, Fe³⁺, Mn³⁺). The second principal component
228 F2 (18.98 % of the eigenvalues) mainly represents the jadeite (Al) and namansilite (Mn³⁺) vs.
229 aegirine (Fe³⁺) substitution.

230 Omphacite always coexists with braunite and piemontite, forming cm-sized boudinaged bands
231 hosted by massive quartz. Braunite crystals can contain included and/or exsolved barite and
232 hollandite (BaMn³⁺₂Mn⁴⁺₆O₁₆), suggesting a possible presence of Ba in the initial braunite. Tumiati

233 et al. (2010) reported up to 194 ppm ($\mu\text{g/g}$) of Ba in these crystals, in addition to other trace
234 elements (e.g. 2015 ppm Cu, 1101 ppm Zn, 272 ppm Sr, 2543 ppm Co and 404 ppm Ni).
235 Piemontite is typically Sr-bearing and shows oscillatory zoning, following the coupled piemontite-
236 (Sr) vs. Fe-epidote substitution. Tumiati et al. (2010) have shown that the Sr-rich parts of
237 piemontite contain up to 459 ppm As, 361 ppm Zn, 937 ppm P, 508 ppm Ni and 767 ppm Ba. In
238 some samples, epidote-group minerals display Mn-poor cores and Mn-rich piemontite rims. The
239 transition between the two compositions is gradual without an obvious solution gap, and follows the
240 substitution $\text{Mn}^{3+}_{+2}\text{Al}^{3+}_{-1}\text{Fe}^{3+}_{-1}$.

241 Garnet is a solid solution of spessartine and grossular with minor contents in calderite
242 ($\text{Mn}^{2+}_3\text{Fe}^{3+}_2\text{Si}_3\text{O}_{12}$) and pyrope. The garnet crystals are generally only slightly zoned in these levels.

243

244 5.2 High-P veins

245 Veins crosscutting the basal levels are quartz-rich and contain piemontite, omphacite, braunite (Fig.
246 4b; Table 1), pyroxmangite and hematite. Piemontite is euhedral and commonly displays oscillatory
247 zoning with REE and Sr substituting for Mn following the exchange $2 \text{Ca}^{2+}_A + 1 \text{Mn}^{3+}_M = 2 \text{Sr}^{2+}_A +$
248 1REE^{3+}_M (first eigenvector of the PCA; 80.4% of the total eigenvalues). The maximum contents in
249 REE and Sr observed are 0.24 atoms per formula unit (a.p.f.u.) ($\text{Ce/La} = 2.36$) and 0.17 a.p.f.u.,
250 respectively (for 12.5 equivalent O). These oscillatory zones are sharp and superimposed to a
251 weaker and more regular zoning involving Fe^{3+} vs. Mn^{3+} , suggesting an increase of the piemontite
252 endmember from core to rim (second eigenvector of the PCA; 15.0% of the total eigenvalues).

253 Veins often contain pink Mn-bearing phengite, known as *alurgite*. Occasionally, As and Sb silicates
254 and oxides occur, in particular ardennite (a rare hydrous silico-arsenate of aluminium and
255 manganese; Fig. 6B) and the calcium antimonate romeite (Fig. 6c).

256 A quartz-rich vein, between the basal braunite/piemontite-rich and the upper garnet-rich levels (Fig.
257 3), contains emerald-green omphacite (Jd_{70}), minor Cr-rich phengite and (Cr, REE)-rich epidote-
258 group minerals. Accessory minerals are Cr-bearing hematite (up to 3.51 wt% Cr_2O_3) and braunite

259 (up to 0.52 wt% Cr₂O₃). As-bearing apatite (up to 9.22 wt% As₂O₃), native Au and REE-vanadates
260 (wakefieldite; M. Merlini pers. comm.; details provided elsewhere) have been found as accessory
261 phases.

262

263 5.3 Upper levels

264 Upper levels (Fig. 3; Table 1) are dominated by garnet and quartz associated with hematite,
265 pyroxmangite (Fig. 4c; see Raman spectrum of sample 1601 in Fig. 5) and/or an aegirine-rich Mn-
266 bearing clinopyroxene known as *schefferite*. Garnet is zoned with grossular- and/or calderite-rich
267 core and spessartine-rich rim (cf. also Cenki-Tok and Chopin, 2006). In the Fe³⁺-rich core, Cr is
268 present up to Uv_{1.1} (0.022 a.p.f.u. per 12 equivalent O; 0.32 wt% Cr₂O₃). The epidote-group mineral
269 manganiandrosite-(Ce) occurs instead of piemontite as an accessory phase (Cenki-Tok et al. 2006).
270 Sb-rich pyrophanite (MnTiO₃) was also observed (Fig. 6d).

271 In one sample, dominated by tephroite, hausmannite and rhodochrosite, we observed a peculiar
272 quartz-free assemblage, where braunite and pyroxmangite show resorption microstructures (Fig. 4d;
273 Table 1).

274

275 6. Thermodynamic modelling

276 At Praborna, the occurrence of omphacite + quartz and of pyroxmangite (e.g. Maresch and Mottana,
277 1979) confirms that these Mn-rich metasediments equilibrated at HP conditions in the eclogite
278 facies. Jadeite-rich omphacite in equilibrium with quartz occurs also in the pervasive veins that
279 crosscut the basal layers, suggesting that an interaction with vein-forming fluids occurred also at
280 HP. These fluids are likely derived from the dehydration of the slab and flushed the mélange rocks,
281 like the serpentinite and glaucophanite now cropping out at the bottom of the sequence. This is the
282 best of all possible environments to be considered, for verifying the mobility of the component
283 oxygen in the slab. The importance of fO_2 in controlling the phase relationships of Mn-rich systems
284 was first recognised by Muan (1959) and Huebner (1967), who demonstrated that, analogously to

285 the Fe–O system, Mn-oxides can be used as oxygen buffers because Mn shows changes in the
286 oxidation state from +2 to +4. Also, the presence of piemontite requires very high fO_2 to be
287 stabilized over garnet, as experimentally demonstrated by Anastasiou and Langer (1977), and
288 Keskinen and Liou (1979). However, such systems have been rarely adopted as redox sensors in HP
289 rocks, because the available experimental data are currently restricted to the MnO–SiO₂–O₂ and
290 Al₂O₃–MnO–SiO₂–O₂ systems at 0.4–2.5 GPa (Abs-Wurmbach et al., 1983; Abs-Wurmbach and
291 Peters, 1999).

292 At Praborna, the basal levels are characterised by the assemblage braunite + quartz, the stability of
293 which requires very high fO_2 ($\Delta FMQ = \log (fO_2^{\text{sample}} / fO_2^{\text{fayalite+magnetite+quartz}}) = +11$ at 0.8 GPa and
294 500 °C, estimated by Brown et al., 1978). These high fO_2 values have been interpreted as indicative
295 of highly oxidized rocks, inheriting the fO_2 of the sedimentary protolith. In this section, we quantify
296 the μO_2 , fO_2 and nO_2 variables at Praborna, using a specific thermodynamical dataset customized
297 for Mn-rich systems and presented in Appendix.

298

299 *6.1 Modelling of the MnO–SiO₂–O₂ system*

300 The MnO–SiO₂–O₂ is the simplest petrological system that describes the phase relations between
301 Mn-silicates and oxides. Pure phases belonging to this system are: quartz, manganosite (Mn²⁺O),
302 tephroite (Mn²⁺₂SiO₄), pyroxmangite (Mn²⁺SiO₃), rhodonite (Mn²⁺SiO₃), hausmannite
303 (Mn²⁺Mn³⁺₂O₄), braunite (Mn²⁺Mn³⁺₆SiO₁₂), bixbyite (Mn³⁺₂O₃) and pyrolusite (Mn⁴⁺O₂). Solid
304 solutions are not expected in this system. Using literature (Table A-1 in Appendix) and new
305 experimentally derived thermodynamic data for these phases (Table A-2 and A-3 Appendix), we
306 were able to construct two diagrams (Figs. 7a and 7b), calculated at $P = 2.1$ GPa and $T = 550$ °C,
307 i.e. at the metamorphic conditions recorded by the slab lithologies in the Saint-Marcel valley
308 (Martin et al., 2008). Diagrams 7a and 7b consider, respectively, the component O₂ as “perfectly
309 mobile” (i.e., μO_2 and fO_2 are intensive independent state variables) and “inert” (nO_2 is an extensive
310 independent state variable). We recall that in these diagrams and in the following calculations, nO_2

311 is set to zero value for rocks in which all Fe and Mn occur exclusively in their divalent oxidation
312 state. Therefore, nO_2 could be regarded as extra moles of the component O_2 relative to a Fe^{3+} - and
313 Mn^{3+} -free reference composition (see also Section 2).

314 Figure 7a displays $\log (fO_2/1 \text{ bar}) - \mu O_2$ vs. X_{SiO_2} ($=SiO_2/(Mn^{2+}O+SiO_2)$). The bulk Mn^{3+}/Mn_{tot}
315 ratio is also reported (shaded areas in Fig. 7a and black dotted isopleths in Fig. 7b). For comparison,
316 reference redox buffers, such as, hematite + magnetite, pyrite + Fe-sulphate and piemontite + garnet
317 are shown in Figure 7a, where they are expressed as ΔFMQ , i.e. with reference to the fayalite +
318 magnetite + quartz buffer (FMQ).

319 The braunite + quartz + pyroxmangite assemblage of the basal levels at Praborna is stable for
320 almost the entire X_{SiO_2} range (except for very low SiO_2 contents, where quartz disappears) at very
321 high fO_2 ($\Delta FMQ = +12.7$), above the hematite–magnetite buffer and slightly above the piemontite–
322 garnet buffer. This is consistent with the occurrence of piemontite and hematite in basal levels
323 (Figs. 4a, b).

324 The upper levels of Praborna are characterised by the equilibrium between pyroxmangite, quartz,
325 garnet and hematite (Figs. 3, 4c), which are stable at $\Delta FMQ < +12.7$ and $X_{SiO_2} > 0.5$ according to
326 Figure 7a. In one quartz-free sample, we observed the assemblage braunite + hausmannite +
327 tephroite (blue fields in Figs. 7a, b; see also Fig. 4d) with relics of pyroxmangite. This latter
328 assemblage can be attained only for $X_{SiO_2} < 0.33$ and $\log (fO_2/1 \text{ bar})$ between $FMQ+4.1$ and
329 $FMQ+9.7$. A further constraint is given by the occurrence of sulphates at Praborna (e.g. barite and
330 celestine), and the absence of sulphides. Chalcophile elements, such as Sb and As, partitionate into
331 silicates, phosphates and oxides (Fig. 6), suggesting that the fO_2 at Praborna is higher than the
332 pyrite– $FeSO_4$ buffer (i.e. $\Delta FMQ > +5.7$), even in the most retrograde assemblages. Values of \log
333 $(fO_2/1 \text{ bar})$ in the range from $FMQ+5.7$ to $FMQ+12.7$ widely exceed those previously evaluated for
334 subduction environments (see Introduction and Section 7.2 below).

335 Figure 7b is the ternary chemography of the system $Mn^{2+}O-SiO_2-O_2$. Compositions are portrayed
336 in barycentric mole fractions. This diagram plots the relative positions of the phase assemblages

337 shown in Figure 7a, therefore unravelling the relationships between μO_2 (or $f\text{O}_2$) and the conjugate
338 variable $n\text{O}_2$ (see also Fig. 1). In terms of $n\text{O}_2$, the most reduced possible assemblages (i.e., the
339 poorest in component O_2) consist of tephroite + manganosite, pyroxmangite + tephroite, and quartz
340 + pyroxmangite, depending on $X\text{SiO}_2$ (Fig. 7a). These associations fall on the join $\text{SiO}_2\text{--Mn}^{2+}\text{O}$,
341 where $n\text{O}_2$ is null and $\text{Mn}^{3+}/\text{Mn}_{\text{tot}} = 0$. On the other hand, the most oxidized assemblage (i.e., the
342 richest in component O_2) is braunite + bixbyite, for which $n\text{O}_2$ and $\text{Mn}^{3+}/\text{Mn}_{\text{tot}}$ range from 0.16 to
343 0.20 and from 0.86 to 1.00, respectively, depending on the phase proportions. The assemblage
344 bixbyite + hausmannite and bixbyite + hausmannite + braunite can therefore have the same
345 $\text{Mn}^{3+}/\text{Mn}_{\text{tot}}$ ratio, provided that the abundance of hausmannite is sufficiently low. The $\text{Mn}^{3+}/\text{Mn}_{\text{tot}}$
346 ratio and $n\text{O}_2$ values are directly proportional only on the $\text{Mn}^{2+}\text{O--O}_2$ subspace of the chemographic
347 diagram. As a consequence, the equilibrium tie-lines of Figure 7b, which delimit the phase fields
348 with identical chemical potentials, crosscut the $n\text{O}_2$ and $\text{Mn}^{3+}/\text{Mn}_{\text{tot}}$ isopleths at high angle. This
349 translates into a decoupling between μO_2 , $n\text{O}_2$ and $\text{Mn}^{3+}/\text{Mn}_{\text{tot}}$, when comparing Figures 7a and 7b.
350 To better understand this concept, we reported a hypothetical metasomatic path represented by the
351 black arrow of Figure 7b. Evolution of the bulk composition along this path from the starting point
352 to the ending point induces a change of the assemblage hausmannite + braunite + tephroite (blue
353 field: $\text{Mn}^{3+}/\text{Mn}_{\text{tot}} = 0.70$; $\mu\text{O}_2 = -267 \text{ kJ}\cdot\text{mol}^{-1}$; $n\text{O}_2 = 0.13$) to the assemblage braunite +
354 pyroxmangite + quartz (red field: $\text{Mn}^{3+}/\text{Mn}_{\text{tot}} = 0.30$; $\mu\text{O}_2 = -219 \text{ kJ}\cdot\text{mol}^{-1}$; $n\text{O}_2 = 0.03$). Counter-
355 intuitively, it is therefore possible to *increase* μO_2 (and $f\text{O}_2$), while $n\text{O}_2$ and $\text{Mn}^{3+}/\text{Mn}_{\text{tot}}$ actually
356 *decrease*. In this case, oxidation in terms of an increase of the intensive variable μO_2 (or $f\text{O}_2$)
357 actually corresponds to a decrease in $n\text{O}_2$ and $\text{Mn}^{3+}/\text{Mn}_{\text{tot}}$, and thus to a bulk reduction. The
358 $\text{Mn}^{3+}/\text{Mn}_{\text{tot}}$ ratio is also depicted in Figure 7a by greyscale tones grading from black ($\text{Mn}^{3+}/\text{Mn}_{\text{tot}} =$
359 1) to white ($\text{Mn}^{3+}/\text{Mn}_{\text{tot}} = 0$), showing that the same $\text{Mn}^{3+}/\text{Mn}_{\text{tot}}$ ratio can be found at different μO_2
360 conditions. Figures 7a and 7b show that the decrease in $f\text{O}_2$ from the basal (red) to the upper (blue)
361 levels of Praborna does not necessarily correspond to an increase in bulk $\text{Mn}^{3+}/\text{Mn}_{\text{tot}}$ as one would
362 expect. The $\text{Mn}^{3+}/\text{Mn}_{\text{tot}}$ ratio is also a function of phase abundances, which cannot be evaluated

363 using μO_2 (or $f\text{O}_2$) diagrams. Therefore, the high $f\text{O}_2$ values observed at Praborna cannot be
364 considered a straightforward sign of high degrees of oxidation.

365

366 6.2 Comparison with the $\text{FeO-SiO}_2\text{-O}_2$ system

367 The peculiarity of the $\text{MnO-SiO}_2\text{-O}_2$ system is mostly related to the occurrence of braunite, a
368 compound that does not have an analogue in the well known $\text{FeO-SiO}_2\text{-O}_2$ system. In order to
369 explore differences and similarities between Mn- and Fe-bearing assemblages, we have constructed
370 a four-component, $\text{FeO-MnO-SiO}_2\text{-O}_2$, compositional space shown in Figure 8. Analogously to
371 Figure 7b, also in this diagram the quantity of the component oxygen ($n\text{O}_2$) is treated as an
372 independent state variable, and $f\text{O}_2$ (expressed as ΔFMQ in the figure) is dependent. Every Mn-
373 bearing phase has a corresponding Fe-bearing phase, except braunite. While hematite and magnetite
374 can coexist with quartz, hausmannite and bixbyite cannot, because of the stability of braunite. In
375 Figure 8, the high- $f\text{O}_2$ phase assemblage braunite + pyroxmangite + quartz + hematite of the basal
376 levels (red volume) can be accessed from the low- $f\text{O}_2$ braunite + hausmannite + tephroite +
377 hematite assemblage of the upper levels (blue volume) just by adding silica (e.g. via a metasomatic
378 agent), even decreasing $n\text{O}_2$, similarly to what displayed in Figure 7b. The grey plane in Figure 8
379 represents the surface where $n\text{O}_2$ is constant and is drawn to highlight the decoupling between
380 oxygen intensity ($f\text{O}_2$) and extensity ($n\text{O}_2$). Moving along this plane it is possible to cross ultra-high
381 $f\text{O}_2$ (e.g. red volume, $\Delta\text{FMQ} = +12.7$) and ultra-low $f\text{O}_2$ (e.g. light green, $\Delta\text{FMQ} = -18.1$)
382 assemblages at constant $n\text{O}_2$, which means without changing the bulk “redox budget” (Evans, 2006)
383 of the rock.

384 Therefore, although the braunite + pyroxmangite + quartz + hematite assemblage of the basal levels
385 of Praborna shows an ultra-oxidized redox state in terms of intensive redox parameters ($\Delta\text{FMQ} =$
386 $+12.7$), it could have the same quantity of O_2 component as magnetite- and even ultra-reduced
387 wüstite-bearing assemblages.

388

389 **7. Discussion**

390 In this section, we re-discuss the concept of oxidation degree of slab rocks, emphasizing the choice
391 between intensive (μO_2 or fO_2) and extensive (nO_2) parameters to describe properly redox
392 conditions. In general, we will demonstrate that the oxidation degree of rocks is definitely a relative
393 concept, dependent on the variable used to describe it.

394

395 *7.1 Oxygen chemical potential versus oxygen molar quantity: is oxygen a “perfectly mobile” or an*
396 *“inert” component?*

397 The rocks of Praborna clearly suggest that even in the presence of pervasive flux of fluids, the
398 homogenization of μO_2 was not attained. In fact, if oxygen had been perfectly mobile, μO_2 (and fO_2)
399 would have been constant but, on the contrary, while the country-rock pyrite-magnetite-bearing
400 glaucophanite records $\Delta FMQ < +2.6$ (Fig. 7a), the adjacent basal Mn-rich quartzites attain ΔFMQ
401 $\geq +12.7$. Moreover, we recognised a mineralogical variability between the basal and upper levels,
402 reflecting ΔFMQ down to +5.7. These observations suggest that, in these rocks, oxygen can hardly
403 be considered a “perfectly mobile” component, as defined by Korzhinskii (1959); thus, the
404 description of the redox conditions of such petrological systems should not be described by μO_2 (or
405 fO_2) as an *independent* state variable. The introduction of its conjugate variable nO_2 is instead
406 required, μO_2 becoming *dependent* of nO_2 . Figures 7a, 7b and 8 warn against the indiscriminating
407 use of μO_2 (or fO_2) as univocal indicator of the redox state of a rock system. Especially in multi-
408 component and metasomatic systems, the nO_2 and μO_2 (or fO_2) could be well decoupled.

409 In order to enlighten this concept, we can make a comparison with a more intuitive analogue: P and
410 V is a couple of intensive and extensive variables similar to μO_2 and nO_2 , respectively. Pressure P
411 (like μO_2 or fO_2) is generally considered as an independent variable imposed upon the system by its
412 environment, to which the system responds by adapting the conjugate variable V (similarly to nO_2),
413 in order to reach the state of equilibrium. However, in a few particular cases, like fluid inclusions, V

414 is imposed by the surroundings, which may induce local P heterogeneities, like overpressures at the
415 inclusion scale; in that case, V should be considered as the independent variable and P the conjugate
416 dependent variable. This occurs when volumes cannot adjust as easily as pressures. In our case,
417 nO_2 , in part inherited from the sedimentary protolith, cannot adjust itself easily – in other terms, O_2
418 not a “perfectly mobile” component. This generates local μO_2 heterogeneities, and nO_2 should be
419 considered as the independent variable that determines the redox state.

420

421 *7.2 Consequences for fO_2 estimates in subduction zones*

422 In a multi-component system, the chemical potential of each component, including oxygen, is
423 ideally homogeneous, i.e. equal in all the phases at equilibrium. As seen in Figures 7a, 7b and 8,
424 different mineralogical associations will be characterised by different chemical potentials, including
425 μO_2 , and thus fO_2 , even when they display the same nO_2 or the same Fe^{3+} and Mn^{3+} contents. In
426 fact, two variables in a conjugate pair, such as μO_2 (or fO_2) and nO_2 , are coupled, i.e. both increase
427 or both decrease, only if all the other molar quantities are kept at constant values. The addition of
428 SiO_2 or FeO components, for example via a metasomatic process, can produce assemblages
429 characterised by different fO_2 without necessarily changing the redox budget. This consideration
430 warns against the indiscriminate comparison of fO_2 data for rocks characterized by different bulk
431 composition or simply by different mineral assemblages, because it may lead to apparent redox
432 heterogeneities, wherever μO_2 cannot be considered as an independent variable (i.e., where O_2 is
433 not “perfectly mobile” and therefore rocks could be not in equilibrium to each other). Therefore,
434 heterogeneities in fO_2 do not necessarily require the mobility of redox species.

435 In subduction zones, fO_2 corresponding to a range of ΔFMQ from 0 to +2 has been estimated on
436 carbonate-bearing mantle-wedge peridotite from the Sulu UHP terrane (China) by Malaspina et al.
437 (2009), whereas eclogites from the same area are characterised by ΔFMQ from +2.5 (Cao et al.,
438 2011; massive lawsonite eclogite) to ca. +4 (Cao et al., 2011; foliated clinozoisite + glaucophane
439 eclogite) and ca. +4.5 (amphibole eclogite; Mattinson et al., 2004). Difference in fO_2 between

440 peridotite and eclogite are reported also in the Western Gneiss Region of Norway, where Malaspina
441 et al. (2010) estimated ΔFMQ of -2–0 for garnet websterites, while Donohue and Essene (2000) and
442 Boundy et al. (2002) estimated ΔFMQ in the range +2.5– +3.0 for eclogite-facies marbles.

443 Although it is unclear, at present, whether heterogeneities in $f\text{O}_2$ in the slab (see also Foley, 2011)
444 should be ascribable to differences in chemical–mineralogical composition, to lack of μO_2
445 equilibration, or to differences in redox budget, the case of Praborna appears paradigmatic and
446 suggests that metasomatic processes could lead to ultra-high $f\text{O}_2$ conditions despite a modest, if any,
447 bulk oxidation in terms of $n\text{O}_2$,

448 In order to compare the Praborna metasediments with other slab rocks and the corresponding
449 mantle wedge, we need to evaluate the oxidation states of representative rocks in terms of $n\text{O}_2$.

450 Unlike for μO_2 (or $f\text{O}_2$), the quantification of $n\text{O}_2$ depends on the mineral abundances. Typically,
451 $n\text{O}_2$ may vary in an oxygen buffer assemblages (i.e., oxygen can be added or subtracted) without a
452 change of μO_2 (or $f\text{O}_2$). For example, the addition of oxygen to a hematite + magnetite assemblage
453 leads thus to an increase in the abundance of hematite, an increase of $\text{Fe}^{3+}/\text{Fe}_{\text{tot}}$ and an increase of
454 $n\text{O}_2$, without changing $f\text{O}_2$, as long as both minerals are present. The system is therefore buffered at
455 constant $f\text{O}_2$ (and μO_2).

456 Estimates of $n\text{O}_2$ provided below take into account the mineral mode in different subduction-related
457 rock types. They should be regarded as an attempt to assess the magnitude of the redox budget of
458 the subducting slab pile and its overlying mantle wedge. Concerning HP rocks, only few analytical
459 data allowing a mass balance of the component oxygen are reported in literature. We profit of the
460 case of HP rocks from Sulu (China), a unique region where the Fe^{3+} contents of garnet and
461 clinopyroxene have been measured both in wedge peridotite (Malaspina et al., 2009; 2012) and in
462 slab eclogite (Proyer et al., 2004).

463 For peridotite mineral assemblages, the contribution of garnet to $n\text{O}_2$ (cf. Fig. 7b and 8) is the
464 amount of excess oxygen with reference to a Fe^{3+} -free system, provided by the skiaegite
465 ($\text{Fe}^{3+}_2\text{Fe}^{2+}_3\text{Si}_3\text{O}_{12}$) component. In the following idealized mass balance, oxygen (O_2) is not regarded

466 as a phase or species but merely as a component and therefore can be made explicit:

467

468 $1.00 \times (\text{FeO})_{0.59} \cdot (\text{SiO}_2)_{0.35} \cdot (\text{O}_2)_{0.06}$ [skiagite] =

469 $0.71 \times (\text{FeO})_{0.67} \cdot (\text{SiO}_2)_{0.33}$ [fayalite] + $0.24 \times (\text{FeO})_{0.50} \cdot (\text{SiO}_2)_{0.50}$ [ferrosilite] + 0.06 O_2 (Eq. 1).

470

471 This equation, after Luth et al. (1990), has been rewritten here expressing compounds as molar
472 fractions of the independent components SiO₂, FeO, MnO and O₂ (see Section 2; Spear et al.,
473 1982), allowing a direct comparison of the excess O₂ with different barycentric representations
474 (Figs. 7b and 8). In the discussion below, we will use the same convention to express chemical
475 compositions of minerals and rocks.

476 According to Eq. 1, one mole of pure skiagite would lead to 0.06 mole of excess O₂. Because
477 Malaspina et al. (2009) reported garnet containing up to 6 mol% of skiagite, one mole of garnet
478 from Sulu peridotite contributes for the 6 percent of 0.06 mole of O₂, i.e. for 3.6 millimoles of
479 excess O₂.

480 In mafic eclogites, a model redox mass balance for skiagite can be written as:

481

482 $1.00 \times (\text{FeO})_{0.59} \cdot (\text{SiO}_2)_{0.35} \cdot (\text{O}_2)_{0.06}$ [skiagite] = $+1.37 \times (\text{FeO})_{0.43} \cdot (\text{Al}_2\text{O}_3)_{0.14} \cdot (\text{SiO}_2)_{0.43}$ [almandine] -

483 $0.39 \times (\text{Al}_2\text{O}_3)_{0.5} \cdot (\text{SiO}_2)_{0.5}$ [kyanite] - 0.04 SiO_2 [quartz/coesite] + 0.06 O_2 (Eq. 2).

484

485 The coefficients for O₂ are the same in Equations 1 and 2, suggesting that in both mafic and
486 ultramafic rocks the excess oxygen is 0.06 mole of O₂ per 1 mole of skiagite component.

487 Profiting of the garnet composition reported by Proyer et al. (2004), containing up to 5 mol% of
488 skiagite, the contribution of one mole of garnet from Sulu eclogite is therefore the 5 percent of 0.06
489 moles of O₂ (v. Eq. 2), i.e. 3.0 millimoles of excess O₂ per 1 mole of garnet.

490 As peridotitic and eclogitic garnets display comparable skiagite content (~5% in eclogite and ~6%
491 in peridotite), the *n*O₂s for one mole of garnet are also comparable (3.6 and 3.0 millimoles in

492 peridotite and eclogite, respectively).

493 The contribution of clinopyroxene to the bulk oxidation can be evaluated on the basis of the
494 aegirine ($\text{NaFe}^{3+}\text{Si}_2\text{O}_6$) component, which can be expressed in the following way, for peridotite
495 (Eq. 3) and eclogite (Eq. 4) assemblages respectively.

496

497 $1.00 \times (\text{Na}_2\text{O})_{0.13} \cdot (\text{FeO})_{0.27} \cdot (\text{SiO}_2)_{0.53} \cdot (\text{O}_2)_{0.07}$ [aegirine] = $0.80 \times (\text{Na}_2\text{O})_{0.17} \cdot (\text{Al}_2\text{O}_3)_{0.17} \cdot (\text{SiO}_2)_{0.67}$
498 [jadeite] - $0.80 \times (\text{FeO})_{0.50} \cdot (\text{SiO}_2)_{0.50}$ [ferrosilite] + $0.13 \times (\text{FeO})_{1.00} \cdot (\text{SiO}_2)_{1.00} \cdot (\text{Al}_2\text{O}_3)_{-1.00}$ [Fe
499 Tschermak] + $0.80 \times (\text{FeO})_{0.67} \cdot (\text{SiO}_2)_{0.33}$ [fayalite] + 0.07 O_2 (Eq. 3).

500

501 $1.00 \times (\text{Na}_2\text{O})_{0.13} \cdot (\text{FeO})_{0.27} \cdot (\text{SiO}_2)_{0.53} \cdot (\text{O}_2)_{0.07}$ [aegirine] = $0.80 \times (\text{Na}_2\text{O})_{0.17} \cdot (\text{Al}_2\text{O}_3)_{0.17} \cdot (\text{SiO}_2)_{0.67}$
502 [jadeite] + $0.53 \times (\text{FeO})_{0.50} \cdot (\text{SiO}_2)_{0.50}$ [ferrosilite] - 0.13 SiO_2 [quartz/coesite] - $0.27 \times$
503 $(\text{Al}_2\text{O}_3)_{0.5} \cdot (\text{SiO}_2)_{0.5}$ [kyanite] + 0.07 O_2 (Eq. 4).

504

505 Similarly to equalities involving garnet in Equations 1 and 2, the coefficients of O_2 in Equations 3
506 and 4 are identical and independent on the system chosen, accounting for 0.07 mole of excess O_2
507 per 1 mole of pure aegirine. Clinopyroxene from Sulu peridotite contains 5 mol% of aegirine
508 endmember (Malaspina et al., 2012), while clinopyroxene from eclogite contains 6 mol% of
509 aegirine (Proyer et al., 2004). Therefore, one mole of clinopyroxene contributes to 3.5 and to 4.2
510 millimoles of excess O_2 in peridotites and mafic eclogites, respectively.

511 On the basis of the above considerations, a bimineralic eclogite composed of 50 mol% of garnet and
512 50 mol% of clinopyroxene would be characterized by 3.6 millimoles of excess O_2 per mole of a
513 rock, whose composition is expressed as molar fractions of oxides. On the other hand, assuming 5
514 mol% of garnet and 5 mol% of clinopyroxene, a peridotite would be characterized by 0.36
515 millimoles of excess O_2 per mole of rock, which means one order of magnitude less.

516 Metasedimentary rocks at Praborna display $n\text{O}_2$ that can be estimated on the basis of the
517 proportions between pyroxmangite, braunite and quartz (see Fig. 7b). Considering the bulk

518 chemical and mineralogical compositions reported by Tumiati et al. (2010), we estimated average
519 contents of ca. 95 mol% of quartz and 5 mol% of pyroxmangite + braunite. Although the available
520 data are not sufficient to determine the pyroxmangite/braunite ratio, we can estimate that the
521 braunite abundance equals that of pyroxmangite, being the first mineral more abundant in the basal
522 levels and the second in the upper levels. Braunite and pyroxmangite can be written respectively as
523 $(\text{MnO})_{0.74} \cdot (\text{SiO}_2)_{0.11} \cdot (\text{O}_2)_{0.16}$ and $(\text{MnO})_{0.50} \cdot (\text{SiO}_2)_{0.50}$ (see Fig. 7b). Therefore, only braunite can
524 contribute to the excess O_2 of the Mn-rich metasediments of Praborna, at the rate of 2.5% of 0.16
525 moles of excess O_2 , i.e. 4.0 millimoles of excess O_2 per 1 mole of rock. This value is nearly
526 identical to the excess O_2 of the Sulu eclogite, suggesting that the Mn-rich metasediments of a
527 subduction mélange can display towards the mantle an oxidizing power comparable to that of slab
528 rocks, despite the presence of ultra-high $f\text{O}_2$ mineral assemblages.

529 As a consequence, a likely scenario for the slab-mantle interface in natural geodynamic
530 environments is illustrated in Figure 9. Mass transport and metasomatism are supported by
531 chemical gradients, notably by gradient in $n\text{O}_2$ across rocks of the subduction channel towards the
532 mantle hanging-wall. Dehydration processes trigger fluid flow, which is localized in shear zones,
533 and open fractures and pervasive microfractures. While ΔFMQ is likely very inhomogeneous,
534 reflecting the different bulk chemical–mineralogical compositions and the limited mobility of
535 oxygen, the oxidation degree of the subduction channel, expressed in terms of $n\text{O}_2$, is expected to
536 be much smoother. In the conceptual model of Figure 9, a sort of metasomatic front develops from
537 the slab to the overlying mantle wedge passing through a transitional layer of mélange rocks.
538 Although fluids cannot transport oxygen as a major volatile species, they are expected to promote
539 mass transfers and to affect the attainment of equilibrium and kinetics of reactions (Lasaga and Rye,
540 1993; Marschall and Schumacher, 2012). Therefore, oxygen is expected to be transported,
541 especially along fractures and veins (see inset of Fig. 9), possibly through mechanisms of
542 dissolution-precipitation of O-enriched oxides and silicates. The front is possibly sustained also
543 by the strong inverse thermal gradient across the slab surface, which is evaluated to be in the order

544 of -20 °C/km (Arcay et al., 2007). Whether a thermophoretic effect at the slab–mantle interface is
545 able to contribute to the O₂ component redistribution or mass-transport is driven mainly by
546 chemical potential gradients and to advective processes (e.g., Gerya and Yuen, 2003; Marschall and
547 Schumacher, 2012) is an open challenge for understanding rock diversity at subduction zones.

548

549 **8. Conclusions**

550 Praborna HP veined Mn-rich rocks record environmental conditions typical for a subducting slab
551 setting. Although veining and growth of “pegmatoid” HP minerals might suggest an open system,
552 characterized by large fluid-rock ratios, the extremely high fO_2 deduced from Mn–Fe-rich mineral
553 assemblages clearly indicates that oxygen can hardly be considered as a perfectly mobile
554 component. As a consequence, μO_2 , and therefore fO_2 , should not be regarded as long-range
555 properties, indicative of the redox state of the entire rock column of a subduction zone, from the
556 dehydrating oceanic crust to the overlying mantle wedge. On a more general basis, the comparison
557 of fO_2 retrieved from different bulk compositions and phase assemblages may suggest redox
558 heterogeneities in subduction zones, even if the distribution of oxygen is expected to be much more
559 continuous, ranging from a maximum in the mafic eclogites, derived from the altered oceanic
560 basalts and gabbros, and in the sediments of the slab, down to a minimum in the overlying
561 peridotites of the mantle hanging-wall.

562

563 **Acknowledgements**

564 The authors are indebted to the reviewers H. Marschall and A. Korsakov for their useful
565 suggestions. M. Fialin and A. Risplendente supported the work at EMP. F. Zorzi and S. Carbonin,
566 and N. Masciocchi and G. Tagliabue are acknowledged for the acquisition and the refinement of
567 XRD data of braunite and pyrolusite, respectively. P. Mietto, C. Micaglio and E. A. Perseil are
568 thanked for providing some interesting samples. D. Smith is acknowledged for the access to Raman

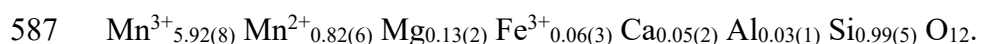
569 facility. This work was supported by the Italian Ministry of Education, University and Research
570 (MIUR) [PRIN-2012R33ECR].

571
572 **Appendix A. Thermodynamic calculations and supplementary data**

573 Phase diagrams of Figures 6 and 7 have been drawn on the basis of thermodynamic calculation
574 performed with the Perple_X computer package (<http://www.perplex.ethz.ch>; Connolly, 1990)
575 using a specifically compiled thermodynamic dataset of Mn-rich minerals and oxygen buffers (see
576 Table A-1). Thermodynamic parameters are available in the literature apart from the thermal
577 expansion coefficients of braunite and pyrolusite, unknown as far as we are aware, and which we
578 derived experimentally from their cell-volume changes during heating (cf. Tables A-2 and A-3).
579 The dataset used has proven to be robust in reproducing the results of the HP experiments of Abs-
580 Wurbach et al. (1983).

581
582 *Thermal expansion of braunite*

583 Braunite at Praborna is invariably polycrystalline. Consequently, powder X-ray diffraction methods
584 rather than single crystal methods were used to measure the thermal expansion of this mineral.
585 Average composition of 11 analyses can be expressed on the basis of 8 cations and 12 O as
586 (standard deviation in parenthesis):



588 Powder diffraction patterns were recorded on a Philips X'Pert PRO automatic powder
589 diffractometer, using a normal focus Cu X-ray tube operating at 40 kV and 40 mA. The vertical
590 goniometer in Bragg-Brentano geometry (with 240 mm radius) was equipped with a first
591 divergence slit, a Soller slit and a 0.2 mm receiving slit upstream of a curved graphite diffracted-
592 beam monochromator PW3123/10. For high temperature data collection, the diffractometer was
593 equipped with a heating camera Anton Paar HTK16.

594 The powder was spread as a thin film directly on the platinum thermocouple (heating strip) and the
595 beam impingement area was restricted to a narrow central section of the strip, so that thermal
596 gradients through and across the sample were minimized. The expansion of Al₂O₃ NIST standard
597 reference material 676 was used for temperature calibration. We estimate the uncertainty of
598 temperature measurement at the sample to be 10 °C.

599 A first data collection performed in continuous mode in the 16–120° 2θ range revealed the good
600 crystallinity and the purity of the phase. Successively, data were collected with a step increment of
601 0.02° and a step counting time of 5 seconds in the 90–120° 2θ range.

602 The position of each Bragg peak was measured by means of “X’pert high score” program and
603 indexed by comparison with the calculated pattern obtained by GSAS program (Larson and Von
604 Dreele, 1994). Angular values and respective crystallographic planes were used to refine lattice
605 parameters *a* and *c* by means of the XLAT program (Rupp, 1988). Diffractometer alignment was
606 repeatedly checked by carrying out data collection of NBS640B silicon standard and obtaining *a*
607 values of 5.4308(1) and 5.4310(1) Å.

608 In Table A-2, we reported the molar volume of braunite at *T* ranging from 25 to 600 °C. These data
609 have been fitted with the expression reported in Table A-1, in order to obtain the volumetric
610 expansion parameter *bl*.

611

612 *Thermal expansion of pyrolusite*

613 Although pyrolusite has proven to be unstable at the investigated conditions, this mineral was
614 included in calculations because it belongs to the investigated petrological system. Thermal
615 expansion data were collected in Bragg-Brentano mode on a Bruker AXS D8 Advance, operating in
616 θ:θ geometry equipped with Nickel filtered Cu-Kα radiation and a position-sensitive Lynxeye
617 detector. Generator settings were 40 kV and 40 mA. Reagent-grade MnO₂ was deposited in the
618 aluminium sample holder of a custom-made heating chamber, operating in air, supplied by *Officine*

619 *Elettrotecniche di Tenno*, Ponte Arche, Italy. A series of scans, lasting ca. 30 min each, were
620 collected in isothermal conditions, in the T range 100–600 °C at 50 °C steps.

621 Cell parameters were refined by the whole pattern structureless refinement technique (Le Bail et al.,
622 1988) with the aid of the TOPAS-R program (V. 3.0, Bruker AXS, Karlsruhe, Germany). Estimated
623 standard deviations were computed under the assumption that, in the absence of systematic effects,
624 errors followed a normal distribution. Similarly to braunite, cell volume data (Table A-3) have been
625 fitted with the expression reported in Table A-1, in order to obtain the volumetric expansion
626 parameter $b1$.

627

628 **References**

629 Abs-Wurmbach, I., Peters, T., Langer, K., Schreyer, W., 1983. Phase relations in the system Mn–
630 Si–O: an experimental petrological study. *Neues Jahrbuch für Mineralogie Abhandlungen*
631 14, 258-279.

632 Abs-Wurmbach, I., Peters, T., 1999. The Mn-Al-Si-O system: an experimental study of phase
633 relations applied to parageneses in manganese-rich ores and rocks. *European Journal of*
634 *Mineralogy* 11, 45-68.

635 Anastasiou, P., Langer, K., 1977. Synthesis and physical properties of piemontite, Ca_2Al_3 -
636 ${}_p\text{Mn}^{3+}(\text{Si}_2\text{O}_7/\text{SiO}_4/\text{O}/\text{OH})$. *Contributions to Mineralogy and Petrology*. 60, 225-245.

637 Arcay, D., Tric, E., Doin, M.P., 2007. Slab surface temperature in subduction zones: Influence of
638 the interpolate decoupling depth and upper plate thinning processes. *Earth and Planetary*
639 *Science Letters* 255, 324-338.

640 Arculus, R.J., 1985. Oxidation status of the mantle—Past and present. *Annual Review of Earth and*
641 *Planetary Sciences* 13, 75–95.

642 Bebout, G.E., 2007. Metamorphic chemical geodynamics of subduction zones. *Earth and Planetary*
643 *Science Letters* 260, 373–393.

- 644 Bebout, G.E., Agard, P., Kobayashi, K., Moriguti, T., Nakamura, E., 2013. Devolatilization history
645 and trace element mobility in deeply subducted sedimentary rocks: Evidence from Western
646 Alps HP/UHP suites. *Chemical Geology* 342, 1-20.
- 647 Bondi, M., Mottana, A., Kurat, G., Rossi, G., 1978. Cristallochimica del violano e della schefferite
648 di St. Marcel (Valle d'Aosta). *Rendiconti della Società Italiana di Mineralogia e Petrologia*.
649 34, 15-25.
- 650 Boundy, T.M., Donohue, C.L., Essene, E.J., Mezger, K., Austrheim, H., 2002. Discovery of
651 eclogite facies carbonate rocks from the Lindås Nappe, Caledonides, Western Norway.
652 *Journal of Metamorphic Geology* 20, 649-667.
- 653 Brown, P., Essene, E.J., Peacor, D., 1978. The mineralogy and petrology of manganese-rich rocks
654 from St. Marcel, Piedmont, Italy. *Contributions to Mineralogy and Petrology*. 67, 227-232.
- 655 Canil, D., 2002. Vanadium in peridotites, mantle redox and tectonic environments: Archean to
656 present. *Earth and Planetary Science Letters* 195, 75–90.
- 657 Cao, Y., Song, S.G., Niu, Y.L., Jung, H., Jin, Z.M., 2011. Variation of mineral composition, fabric
658 and oxygen fugacity from massive to foliated eclogites during exhumation of subducted
659 ocean crust in the North Qilian suture zone, NW China. *Journal of Metamorphic Geology*
660 29, 699-720.
- 661 Castello, P., 1982. Il giacimento di Praborna (S. Marcel-AO). *Rivista Mineralogica Italiana*. 3, 87-
662 92.
- 663 Cenko-Tok, B., Ragu, A., Armbruster, T., Chopin, C., Medenbach, O., 2006. New Mn- and rare-
664 earth-rich epidote-group minerals in metacherts: manganiandrosite-(Ce) and
665 vanadoandrosite-(Ce). *European Journal of Mineralogy* 18, 569–582.
- 666 Cenko-Tok, B., Chopin, C., 2006. Coexisting calderite and spessartine garnets in eclogite-facies
667 metacherts of the Western Alps. *Mineralogy and Petrology* 88, 47-68.
- 668 Chinner, G. A., 1960. Pelitic gneisses with varying ferrous/ferric ratios from Glen Clova, Angus,
669 Scotland. *Journal of Petrology* 1, 178-217.

670 Ciriotti, M. E., Fascio, L., Pasero, M., 2009. Italian type minerals: Edizioni Plus, Pisa.

671 Connolly, J.A.D., 1990. Multi-variable phase diagrams: an algorithm based on generalized
672 thermodynamics. *American Journal of Science* 290, 666-718.

673 Dal Piaz, G.V., 2001. History of tectonic interpretations of the Alps. *J. Geodyn.* 32, 99-114.

674 Dapiaggi, M., Tiano, W., Artioli, G., Sanson, A., Fornasini, P., 2003. The thermal behaviour of
675 cuprite: An XRD-EXAFS combined approach. *Nuclear Instruments and Methods in Physics
676 Research B* 200, 231-236.

677 Dasgupta, S., 1997. P-T-X relationships during metamorphism of manganese-rich sediments:
678 Current status and future studies. *Geological Society Special Publication* 199, 327-337.

679 Donohue, C.L., Essene, E.J., 2000. An oxygen barometer with the assemblage garnet-epidote. *Earth
680 and Planetary Science Letters* 181, 459-472.

681 Evans, K.A., 2006. Redox decoupling and redox budgets: Conceptual tools for the study of earth
682 systems. *Geology*. 34, 489-492.

683 Evans, K.A., 2012. The redox budget of subduction zones. *Earth-Science Reviews* 113, 11-32.

684 Foley, S., 2011. A reappraisal of redox melting in the Earth's mantle as a function of tectonic
685 setting and time. *Journal of Petrology* 52, 1363-1391.

686 Frezzotti, M.L., Selverstone, J., Sharp, Z.D., Compagnoni, R., 2011. Carbonate dissolution during
687 subduction revealed by diamond-bearing rocks from the Alps. *Nature Geosciences* 4, 703-
688 706.

689 Geller, S., Espinosa, G.P., 1970. Magnetic and crystallographic transitions in Sc^{3+} , Cr^{3+} , and Ga^{3+}
690 substituted Mn_2O_3 . *Physical Review B* 1, 3763-3769.

691 Gerya, T., Yuen, D.A., 2003. Rayleigh-Taylor instabilities from hydration and melting propel 'cold
692 plumes' at subduction zones. *Earth and Planetary Science Letters* 212, 47-62.

693 Gill, J., 1981. *Orogenic Andesites and Plate Tectonics*: New York, Springer-Verlag.

694 Greeff, C.W., Boettger, J.C., Graf, M.J., Johnson, J.D., 2006. Theoretical investigation of the Cu
695 EOS standard. *Journal of Physics and Chemistry of Solids* 67, 2033-2040.

- 696 Groppo, C., Castelli, D., 2010. Prograde P-T Evolution of a Lawsonite Eclogite from the Monviso
697 Meta-ophiolite (Western Alps): Dehydration and Redox Reactions during Subduction of
698 Oceanic FeTi-oxide Gabbro. *Journal of Petrology* 51, 2489-2514.
- 699 Hazen, R.M., 1985. Comparative crystal chemistry and the polyhedral approach. *Reviews in*
700 *Mineralogy* 14, 317-345.
- 701 Heines, J., Leger, J.M., Hoyau, S., 1995. 2nd-order rutile-type to CaCl₂-type phase-transition in
702 beta-MnO₂ at high-pressure. *Journal of Physics and Chemistry of Solids* 56, 965-973.
- 703 Hillert, M., 1985. Principles of phase diagrams. *International Metals Review* 30, 45-67.
- 704 Hirschmann, M.M., 2009. Ironing out the oxidation state of Earth's mantle. *Science* 325, 545–546.
- 705 Holland, T.J.B., 1989. Dependence of entropy on volume for silicate and oxide minerals: A review
706 and a predictive model. *American Mineralogist* 74, 5-13.
- 707 Holland, T.J.B., Powell, R., 1998. An internally consistent thermodynamic data set for phases of
708 petrological interest. *Journal of Metamorphic Geology* 16, 309-343.
- 709 Huebner, J., 1967. Stability relations of minerals in the system Mn–Si–C–O [Ph.D. thesis]:
710 Baltimore, John Hopkins University.
- 711 Irani, K.S., Sinha, A.P.B., Biswas, A.B., 1958. Entropy of hausmannite to spinel transformation.
712 *Proceedings of the Physical Society* 71, 270-271.
- 713 Kazanc, S., Çiftci, Y.Ö., Çolakoğlu, K., Ozgen, S., 2006. Temperature and pressure dependence of
714 the some elastic and lattice dynamical properties of copper: a molecular dynamics study.
715 *Physica B* 381, 96-102.
- 716 Kelley, K.A., Cottrell, E., 2009. Water and the oxidation state of subduction zone magmas. *Science*
717 325, 605–607.
- 718 Keskinen M., Liou, J.G., 1979. Synthesis and stability relations of Mn-Al piemontite,
719 Ca₂MnAl₂Si₃O₁₂(OH). *American Mineralogist* 64, 317-328.

- 720 Konrad-Schmolke, M., O'Brien, P.J., Zack, T., 2011. Fluid migration above a subducted slab –
721 Constraints on amount, pathways and major element mobility from partially overprinted
722 eclogite-facies rocks (Sesia Zone, Western Alps). *Journal of Petrology* 52, 457-486.
- 723 Korzhinskii, D.S., 1959. Physicochemical basis of the analysis of the paragenesis of minerals: New
724 York, Consultants bureau, inc.
- 725 Krist, P., Bohem, J., Gerber, R., Kelland, D.R., 1992. OGMS of cryogenically enhanced magnetics.
726 *IEEE Transactions on Magnetism* 28, 2412-2414.
- 727 Langer, K., Tillmanns, E., Kersten, M., Almen, H., Arni, R.K., 2002. The crystal chemistry of Mn³⁺
728 in the clino- and ortho-zoisite structure types, Ca₂M³⁺₃[OH/O/SiO₄/Si₂O₇]: A structural and
729 spectroscopic study of some natural piemontites and “thulites” and their synthetic
730 equivalents. *Zeitschrift für Kristallographie* 217, 563-580.
- 731 Larson, A.C., Von Dreele, R.B., 1994. General Structure Analysis System (GSAS): Los Alamos
732 National Laboratory Report LAUR, p. 86-748.
- 733 Lasaga, A.C., Rye, D.M., 1993. Fluid flow and chemical reaction kinetics in metamorphic systems.
734 *American Journal of Science* 293, 361-404.
- 735 Le Bail, A., Duroy, H., Fourquet, J.L., 1988. Ab initio structure determination of LiSbWO₆ by X-
736 ray powder diffraction. *Materials Research Bulletin* 23, 447-452.
- 737 Lee, C.T.A., Leeman, W.P., Canil, D., Li, Z.X.A., 2005. Similar V/Sc systematics in MORB and
738 arc basalts: implications for the oxygen fugacities of their mantle source regions. *Journal of*
739 *Petrology* 46, 2313–2336
- 740 Lee, C.-T.A., Luffi, P., Le Roux, V., Dasgupta, R., Albarede, F., Leeman, W.P., 2010. The redox
741 state of arc mantle using Zn/Fe systematics. *Nature*. 468, 681-685.
- 742 Luth, R.W., Virgo, D., Boyd, F.R., Wood, B. J., 1990. Ferric iron in mantle-derived garnets;
743 implications for thermobarometry and for the oxidation state of the mantle. *Contributions to*
744 *Mineralogy and Petrology*. 104, 56–72.

- 745 Malaspina, N., Poli, S., Fumagalli, P., 2009. The oxidation state of metasomatized mantle wedge:
746 insights from C-O-H-bearing garnet peridotite. *Journal of Petrology* 50, 1533-1552.
- 747 Malaspina, N., Scambelluri, M., Poli, S., Van Roermund, H.L.M., Langenhorst, F., 2010. The
748 oxidation state of mantle wedge majoritic garnet websterites metasomatised by C-bearing
749 subduction fluids. *Earth and Planetary Science Letters* 298, 417–426.
- 750 Malaspina, N., Langenhorst, F., Fumagalli, P., Tumiati S., Poli, S., 2012. Fe³⁺ distribution between
751 garnet and pyroxenes in mantle wedge carbonate-bearing garnet peridotites (Sulu, China)
752 and implications for their oxidation state. *Lithos* 146-147, 11-17.
- 753 Manheim, F.T., 1978. *Marine manganese deposits*. Elsevier, Amsterdam.
- 754 Maresch, W.V., Mottana, A., 1976. The pyroxmangite-rhodonite transformation for the MnSiO₃
755 composition. *Contributions to Mineralogy and Petrology*. 55, 69-79.
- 756 Marschall, H.R., Schumacher, J.C., 2012. Arc magmas sourced from mélange diapirs in subduction
757 zones. *Nature Geosciences* 5, 862-867.
- 758 Martin, S., Kienast, J.-R., 1987. The HP-LT manganeseiferous quartzites of Praborna, Piedmont
759 ophiolite nappe, Italian western Alps. *Schweizerische Mineralogische und Petrographische*
760 *Mitteilungen* 67, 229-360.
- 761 Martin, S., Rebay, G., Kienast, J.-R., Mevel, C., 2008. An eclogitised oceanic palaeo-hydrothermal
762 field from the St. Marcel Valley (Italian Western Alps). *Ofioliti*. 33, 1-15.
- 763 Mattinson, C.G., Zhang, R.Y., Tsujimori, T., Liou, J.G., 2004. Epidote-rich talc-kyanite-phengite
764 eclogites, Sulu terrane, eastern China: *P-T-f*O₂ estimates and the significance of the epidote-
765 talc assemblage in eclogite. *American Mineralogist* 89, 1772-1783.
- 766 McMurdie, H.F., Sullivan B.M., Mauer, F.A., 1950. High-temperature X-ray study of the system
767 Fe₃O₄-Mn₃O₄. *Journal of Research of the National Bureau of Standards*, 45, 35-41.
- 768 Merkel, S., Jephcoat, A.P., Shu, J., Mao, H.K., Gillet, P., Hemley, R.J., 2002. Equation of state,
769 elasticity, and shear strength of pyrite under high pressure. *Physics and Chemistry of*
770 *Minerals* 29, 1-9.

771 Miletich, R., Allan, D.R., Angel, R.J., 1998. Structural control of polyhedral compression in
772 synthetic braunite $\text{Mn}^{2+}\text{Mn}^{3+}_6\text{O}_8\text{SiO}_4$. *Physics and Chemistry of Minerals* 25, 1983-1992.

773 Mori, M., 2002. Irreversible expansion behavior of $\text{Mn}_3\text{O}_{4+\delta}$ spinel and shrinkage behavior of
774 $\text{La}_{0.6}\text{Sr}_{0.4}\text{MnO}_3$ composites with the spinel during thermal cycling in O_2 atmosphere. *Journal*
775 *of the Electrochemical Society* 149, A995-A1000.

776 Muan, A., 1959. Stability relations among some manganese minerals. *American Mineralogist* 44,
777 946-960.

778 Ohashi, M., Tashiro, A., Oomi, G., Maeda, E., Zeng, X.G., 2006. Effect of pressure on the magnetic
779 phase transition in cupric oxide. *Physical Review B* 73, 134421.

780 Paris, E., Ross, C.R., Olijnyk, H., 1992. Mn_3O_4 at high-pressure – a diamond-anvil cell study and a
781 structural modelling. *European Journal of Mineralogy* 4., 87-93.

782 Proyer, A., Dachs, E., McCammon, C., 2004. Pitfalls in geothermobarometry of eclogites: Fe^{3+} and
783 changes in the mineral chemistry of omphacite at ultrahigh pressures. *Contributions to*
784 *Mineralogy and Petrology*. 147, 305-318.

785 Reinecke, T., 1998. Prograde high- to ultrahigh-pressure metamorphism and exhumation of oceanic
786 sediments at Lago di Cignana, Zermatt-Saas Zone, Western Alps. *Lithos* 42, 147-189.

787 Robertson, E.C., 1988. Thermal properties of rocks. U. S. Geological Survey Open-File Report, 88-
788 441.

789 Robie, R., Hemingway, B.S., 1995. Thermodynamic properties of minerals and related substances
790 at 298.15 K and 1 bar (10^5 Pascals) pressure and at higher temperatures. U.S. Geological
791 Survey Bulletin 2131, 461 pp.

792 Rupp, B., 1988. XLAT – Least square refinements of cell constants. *Scripta Metallurgica*. 22, 1.

793 Sherman, D.M., 1990. Molecular orbital (SCF-X α -SW) theory of Fe^{2+} - Mn^{3+} , Fe^{3+} - Mn^{2+} charge
794 transfer and magnetic exchange in oxides and silicates. *American Mineralogist* 75, 256-261.

795 Shi, P., 1992. Fluid fugacities and phase equilibria in the Fe-Si-O-H-S system. *American*
796 *Mineralogist* 77, 1050-1066.

797 Smyth, J.R., Jacobsen, S.D., Hazen, R.M., 2000. Comparative crystal chemistry of dense oxide
798 minerals. *Reviews in Mineralogy* 40, 157-186.

799 Spear, F.S., Rumble III, D., Ferry, J.M., 1982. Linear algebraic manipulation of n-dimensional
800 composition space. *Reviews in Mineralogy* 10, 53-104.

801 Tumiati, S., 2005 (A). Geochemistry, mineralogy and petrology of the eclogitized manganese
802 deposit of Praborna (Valle d'Aosta, Western Italian Alps) [Ph.D. thesis]: Università
803 dell'Insubria (Como)–Université Denis Diderot (Paris-7).

804 Tumiati, S., Godard, G., Martin, S., Nimis, P., Mair, V., Boyer, B., 2005 (B). Dissakisite-(La) from
805 the Ulten zone peridotite (Italian Eastern Alps): A new end-member of the epidote group.
806 *American Mineralogist* 90, 1177-1185.

807 Tumiati, S., Godard, G., Masciocchi, N., Martin, S., Monticelli, D., 2008. Environmental factors
808 controlling the precipitation of Cu-bearing hydrotalcite-like compounds from mine waters.
809 The case of the “Eve verda” spring (Aosta Valley, Italy). *European Journal of Mineralogy*
810 20, 73-94.

811 Tumiati, S., Martin, S., Godard, G., 2010. Hydrothermal origin of manganese in the high-pressure
812 ophiolite metasediments of Praborna ore deposit (Aosta Valley, Western Alps). *European*
813 *Journal of Mineralogy* 11, 577-594.

814 Tumiati, S., Fumagalli, P., Tiraboschi, C., Poli, S., 2013. An experimental study on COH-bearing
815 peridotite up to 3.2 GPa and implications for crust-mantle recycling. *Journal of Petrology*
816 54, 453-479.

817 Wang, Z., Pischedda, V., Saxena, S.K., Lazor, P., 2002. X-ray diffraction and Raman spectroscopic
818 study of nanocrystalline CuO under pressures. *Solid State Communications* 121, 275-279.

819 Wood, B.J., Bryndzia, L.T., Johnson, K.E., 1990. Mantle oxidation state and its relation to tectonic
820 environment. *Science*. 248, 337–345.

821 Yamanaka, T., Nagai, T., Okada, T., Fukuda, T., 2005. Structure change of Mn₂O₃ under high
822 pressure and pressure-induced transition. *Zeitschrift für Kristallographie* 220, 938-945.

823

824 **Tables**

825 Table 1: Representative compositions of major minerals forming the assemblages of Praborna
826 occurring in the basal levels, upper levels, HP veins and the SiO₂-undersaturated sample C4.

827 Table A-1: Thermodynamic database used for calculations.

828 Table A-2: *V-T* data of braunite.

829 Table A-3: *V-T* data of pyrolusite.

830

831 **Figure captions**

832 Figure 1: Appearance of two-phase field (A + B) between two one-phase fields (A, B) in a unary
833 system, when the molar quantity $n\text{O}_2$ is introduced instead of its conjugate potential μO_2 . Vertical
834 lines in *b* are isothermal tie-lines accounting for the difference in molar quantity $n\text{O}_2$. Redrawn
835 from Hillert (1985).

836

837 Figure 2. Geological sketch map of the Saint-Marcel valley showing the Praborna mine (45.6796°
838 lat. N; 7.4495° long. E) and the principal lithologies occurring in the area.

839

840 Figure 3. Schematic section of the Mn ore. Basal levels are highly fractured and show pervasive
841 veining. The enlargement shows a stockwork of quartz- and feldspar-filled veins cutting the
842 massive ore mainly consisting of braunite (black) and piemontite (purple) (orange crusts are
843 lichens). Note that the growth of “pegmatoid” piemontite crystals is perpendicular to the fracture
844 walls (black arrow). Basal levels and veins contain omphacite in equilibrium with quartz and are in
845 contact with glaucophanites. The upper part of the ore gradates into garnet + quartz ± pyroxmangite
846 assemblages, and is overlaid by Mn-poor micaschists.

847

848 Figure 4. Representative mineral assemblages characterizing the Mn ore of Praborna. (a) Colorized
849 Back Scattered Electron (CBSE) image of braunite (blue), pyroxmangite (green) and hematite
850 (violet) coexisting with quartz in the basal level. (b) Transmitted Light Photomicrograph (TLP) of
851 the vein containing Mn-rich purple omphacite (violan) in equilibrium with quartz, braunite and
852 piemontite. (c) TLP of hematite in equilibrium with garnet, pyroxmangite and quartz in the silica-
853 rich assemblages of the upper level. (d) CBSE image of quartz-free sample from the upper level,
854 showing the replacement of pyroxmangite (yellow) + braunite (blue) by tephroite (blue-green) and
855 hausmannite (violet). Rhodochrosite (red) is a late mineral.

856

857 Figure 5. Raman spectra of MnSiO_3 in selected samples (basal levels: SM93; upper levels: 16/01)
858 compared with those of reference pyroxmangite and rhodonite from the mineralogical collection of
859 the *Muséum National d'Histoire Naturelle* in Paris. These spectra show that MnSiO_3 at Praborna is
860 the high-pressure pyroxmangite polymorph.

861

862 Figure 6. As- and Sb-bearing minerals characterizing the parageneses at Praborna. (a) basal levels;
863 zoned apatite crystal richer in As at the rim (cathodoluminescence image); (b) basal levels;
864 ardenite-(As) $(\text{Mn,Ca,Mg})_4(\text{Al,Mg,Fe})_6(\text{SiO}_4)_2(\text{Si}_3\text{O}_{10})(\text{AsO}_4,\text{VO}_4)(\text{OH})_6$ in equilibrium with
865 garnet and rutile showing a Sb-rich rim (BSE image); (c) basal levels; romeite
866 $(\text{Ca,Fe,Mn,Na})_2(\text{Sb,Ti})_2\text{O}_6(\text{O,OH,F})$ showing oscillatory zoning (BSE image); (d) upper levels;
867 hematite associated to Sb-rich pyrophanite (MnTiO_3) (BSE image).

868

869 Figure 7. Thermodynamic model of the system $\text{MnO-SiO}_2\text{-O}_2$, calculated for $P = 2.1$ GPa and $T =$
870 550 °C. (a) μO_2 ($\text{kJ}\cdot\text{mol}^{-1}$) and $\log(f\text{O}_2/1 \text{ bar})$ vs. $\text{SiO}_2/(\text{MnO}+\text{SiO}_2)$ phase diagram. Compositions
871 are represented in barycentric mole fractions. Considered phases are: quartz (qtz); manganosite
872 (mang); pyroxmangite (pxmn); tephroite (teph); hausmannite (hsm); braunite (braun); bixbyite
873 (bxb); pyrolusite (not stable at these conditions). In addition to μO_2 (right vertical axis), the

874 corresponding $\log (f\text{O}_2/1 \text{ bar})$ and ΔFMQ values (black and grey numbers, respectively, on the left
875 vertical axis) are also reported for comparison. Dashed grey lines are the univariant equilibria
876 piemontite = garnet + H_2O + O_2 , $\text{CuO} = \text{Cu}_2\text{O} + \text{O}_2$, $\text{Cu}_2\text{O} = \text{Cu} + \text{O}_2$, $\text{FeSO}_4 = \text{pyrite} + \text{hematite} +$
877 O_2 , hematite = magnetite + O_2 , and magnetite + quartz = fayalite + O_2 . The red and blue horizontal
878 lines indicate the associations quartz–braunite–pyroxmangite (basal levels) and braunite–
879 haussmanite–tephroite (upper levels), respectively. Shaded fields represents in grey scale the ratio
880 $\text{Mn}^{3+}/\text{Mn}_{\text{tot}}$ as suggested by Figure 7b. (b) Ternary chemography of the system $\text{MnO–SiO}_2\text{–O}_2$.
881 Compositions are represented in barycentric mole fractions (i.e., sum of coordinates = 1). The
882 diagram is stretched vertically (the upper O_2 vertex is not shown) in order to highlight the
883 assemblages without oxygen as a free phase. $n\text{O}_2$ represents the excess of O_2 component with
884 reference to the Mn^{3+} -free system $\text{SiO}_2\text{–MnO}$. μO_2 ($\text{kJ}\cdot\text{mol}^{-1}$) is reported for each divariant field.
885 Thick dotted lines are $\text{Mn}^{3+}/\text{Mn}_{\text{tot}}$ isopleths, whereas horizontal dotted lines are $n\text{O}_2$ isopleths. The
886 quartz– O_2 , braunite– O_2 and bixbyite– O_2 tie-line (dotted arrows) are virtual, because O_2 is not
887 thought to be a real phase at these conditions. The coloured fields correspond to the typical
888 Praborna assemblages as in Figure 7a. Black arrow is a hypothetical metasomatic path from SiO_2 -
889 poor to SiO_2 -enriched assemblages, where $n\text{O}_2$ and the ratio $\text{Mn}^{3+}/\text{Mn}_{\text{tot}}$ decrease while μO_2
890 increases.

891

892 Figure 8. Thermodynamic model of the system $\text{MnO–FeO–SiO}_2\text{–O}_2$ calculated for $P = 2.1 \text{ GPa}$ and
893 $T = 550 \text{ }^\circ\text{C}$. Compositions are represented in barycentric mole fractions. $n\text{O}_2$ represents the excess
894 of component O_2 with reference to the Fe^{3+} - and Mn^{3+} -free system $\text{FeO–SiO}_2\text{–MnO}$. ΔFMQ is
895 reported for each 4-phases assemblage (e.g., +12.7 for pyroxmangite–quartz–braunite–hematite).
896 The grey plane represents the locus of points at constant value of $n\text{O}_2$ and intersects all the
897 assemblages, with ΔFMQ ranging from -18.1 (wüstite–fayalite–magnetite–manganosite, light green
898 volume), to +9.7 (tephroite–hausmannite–braunite–hematite, blue volume, upper levels), and to
899 +12.7 (braunite–quartz–pyroxmangite–hematite, red volume, basal levels).

900

901 Figure 9. Oxygen in the subduction channel. Cartoon redrawn after Konrad-Schmolke et al. (2011)
902 showing a patchy and heterogeneous distribution of fO_2 (see ΔFMQ ; see also Fig. 12 in Foley,
903 2011), but a more regular gradient of nO_2 (i.e. the quantity of oxygen in excess compared to Fe^{3+} -
904 and Mn^{3+} -free systems). In terms of nO_2 , the mélange appears as a metasomatic front from the more
905 oxidized slab to the less oxidized mantle wedge. Oxygen can be transported along fractures and
906 veins through dissolution-precipitation of oxides and silicates fluxed by fluids. See text for further
907 details.